Finite element modelling for mitigation of residual stress and distortion in macro-scale powder bed fusion components

Jinbiao Zhou[1,2,3], Richard A. Barrett[1,2,3], Sean B. Leen[1,2,3]

[1]Mechanical Engineering, College of Engineering and Informatics, University of Galway.

[2]Ryan Institute for Environmental, Marine and Energy Research, University of Galway.

[3]I-Form Advanced Manufacturing Research Centre, Ireland.

Abstract

Powder bed fusion (PBF) has attracted significant attention in many applications due to its capability of fabricating complex and customized metal parts. However, the potential for high inherent residual stresses that produce distortion in additive manufacturing (AM) components, prevents more widespread application of the AM technique. Efficient and accurate prediction of residual stress and distortion at component-level (macro-scale) is a complex task. Although process-level (meso-scale) thermo-mechanical simulations have resulted in accurate predictions for small-scale parts, the computational times (typically weeks) and memory requirements for application of such methods to component-level are prohibitive. The main goal of the current study therefore is to present an efficient and accurate finite element (FE) simulation method with detailed validation for PBF manufacture of a complex 3D Inconel 625 benchmark bridge component (macro-scale). The simulation results are successfully validated against the published benchmark experimental measurements from neutron diffraction, X-ray diffraction (XRD), contour method and coordinate measurement machine (CMM) by the National Institute of Standards and Technology (NIST) laboratory. A key additional novelty of the present work is the investigation of the effects of substrate removal and preheating on mitigation of residual stresses and distortions using the validated model. Ultimately, these results will guide the selection of optimal manufacturing protocols and integration of the FE-based AM modelling for industrial application with complex geometries. The ultimate aim of the present work is to facilitate fatigue life prediction of complex geometry AM components including residual stress effects, e.g. conformally-cooled injection moulding dies (for different material than Inconel 625).

Keywords: Additive manufacturing; Powder Bed Fusion; Thermo-mechanical simulation; Residual stress; Distortion

1. Introduction

Powder bed fusion (PBF) is one of several additive manufacturing (AM) technologies for fabricating complex shape, custom-designed components in which a thin layer of metal powder is first laid and then a moving laser (or electron) beam is applied as the heat source to fully melt the metal powder according to the controlled trajectory [1, 2]. However, high inherent tensile residual stress caused by large thermal gradients and cooling rates, which leads to distortions and cracks in the AM part, is a major concern for PBF [3-5]. Tensile residual stress is detrimental to the fatigue performance of manufactured parts [6, 7]. Hence, it is important to understand the effects of component-level geometry on how residual stresses develop during PBF, i.e. not just at the material or process level, and how to mitigate residual stress and distortion induced in components manufactured by PBF.

Previous work on the analysis of residual stresses in PBF has been conducted using experimental and numerical methods [8, 9]. Several experimental measurements have been made to systematically investigate the magnitude of residual stress and distortion during PBF. Simson et al. [10] investigated residual stress in selective laser melting (SLM) samples made from 316L austenitic stainless steel at different depths and on two outer surfaces using X-ray diffraction (XRD), showing that the orientation of the main stress components is dependent on the examined layer. For example, the residual stresses at the top surface are higher in the laser scanning direction than those in the perpendicular direction. Phan et al. [11] conducted high-fidelity residual strain and residual stress benchmark measurements in PBF built Inconel 625 bridge-shaped component using neutron diffraction, XRD and contour method. The distortion of the component was measured using the coordinate measurement machine (CMM). The results using different techniques are in reasonable agreement with each other. These results are used here to validate the proposed new FE-based AM process model for residual stresses, strains and distortions in complex geometries. Barros et al. [12] measured residual stress of PBF Inconel 718 cuboid specimens in the as-built state and after standard solution annealing and ageing heat treatment conditions using the hole-drilling strain-gage method and highlighted that residual stress decreased markedly after the heat treatment. Teixeira et al. [13] have recently presented a detailed review of residual stress development in PBF for Inconel 718 and concluded that although optimized heat treatment can successfully reduce residual stresses for Inconel 718, there are still significant process-structure-property challenges, including investigation of different heat treatment strategies, as investigated in this work for Inconel 625. Mishurova et al. [14] evaluated the effect of the support structure and substrate removal on

residual stress and distortion in SLM Inconel 718 parts by means of XRD and highlighted that (i) the removal from the substrate leads to residual stress redistribution and relaxation on the sample and (ii) the supporting structures between the AM built sample and the substrate are useful for compensating the distortion. However, it is not possible to provide supporting structures in all the areas of printed components, and post-print removal is typically difficult. The effects of preheating on residual stress reduction and mechanical properties enhancement of SLM Ti-6Al-4V were demonstrated experimentally by Ali et al. [15]. The generated residual stresses were 88.3% lower at the component preheated at 470 °C compared to that preheated at 100 °C and the yield strength and elongation of components with 570 °C preheating temperature improved by 3.2% and 66.2%, respectively. In general, experimental methods are time-consuming and cost-intensive for routine assessment of residual stress or design studies to mitigate residual stresses [16]. Accordingly, numerical modelling methods, validated against relevant experimental data, are potentially efficient alternatives to predict residual stress and distortion in AM processes, and to facilitate quick and cost-effective AM design and optimization [17].

In general, existing AM process modelling methods can be categorized into process-level [18-20] and component-level [21-23] models. Detailed process-level modelling has been performed using a small step increment and a fine mesh with at least one element per layer. Hussein et al. [18] proposed a three-dimensional (3D) transient finite element (FE) model to predict the temperature and stress fields within a single 316L stainless steel layer built on the powder bed using the SLM process, revealing differences in temperature and stresses at different locations of the layer, but without explicit comparisons against experimental measurements. Hodge et al. [19] presented a continuum thermo-mechanical modelling method for calculation of the thermal and mechanical history of a SLM manufactured 316L stainless steel cube (12 layers in total) and highlighted the limitations of the Bathe algorithm [24] for phase change modelling due to significant computational resources required. Recently, Yang et al. [20] developed a 3D FE model for predicting the thermal history and spatial distributions of temperature in the PBF process using the 'element birth and death' technique in Abaqus (commonly referred as the 'Model Change' technique [25]), and extended to solid-state phase transformation for Ti-6Al-4V. In this case, the predictions of thermal history and molten pool dimensions were successfully validated against measured data [26]. Although modelling at the process-level can capture the rapidly evolving temperature and details of melt pool process physics, the computational domain is typically small (e.g. only a few layers of thickness) due to high computational cost

[27, 28]. Promoppatum et al. [21] investigated the inherent strain based approach for prediction of residual stresses in PBF Inconel 718 parts, with comparison against neutron diffraction measured results for validation of the developed FE framework. A key limitation of the inherent strain approach is the challenge in determining accurate inherent strain fields since they strongly depend on the AM process parameters. Bayat et al. [22] developed a component-level FE-based thermo-mechanical model for predicting residual stresses and distortions for PBF Ti-6Al-4V, using the flash heating (FH) method as a multi-scaling approach to improve computational efficiency. However, the FH method is insensitive to the scanning strategy, which leads to unrealistic prediction of residual deformation. Williams et al. [23] introduced a pragmatic FE-based component-level model for residual stress and distortion prediction in PBF process. Several layers were combined into a thicker computational section or block in their model, which is based on the 'block dump' approach. For example, 16 layers were amalgamated to a height of 0.8 mm section in the model; the differences between predicted and measured (using digital image correlation (DIC)) distortion were within 5% for the bridge component made from 316L stainless steel. The 'block dump' approach can capture the thermo-mechanical conditions with reasonable accuracy, but high-performance computing is often required. The recently developed AM built-in module of the general-purpose FE software Abaqus [29] (hereafter referred as 'Abaqus AM') was evaluated by Song et al. [9] for both PBF and (Directed Energy Deposition) DED process of Inconel 718; the residual stress predictions from FE simulation captures the trend from the Focused Ion Beam (FIB) slitting + DIC measured results, and the maximum difference between FE predictions and FIB-DIC measurements is about 38.6% (viz. 610 MPa, as compared to 440 MPa). In our previous work [30], a 3D FE model using Abaqus AM was developed to predict thermal histories and residual stresses in a realistic DED Ti-6Al-4V component.

The objectives of the present study are (i) to develop and validate an efficient and accurate process simulation model for component-level PBF, based on benchmark experimental test data, and (ii) to investigate the application of this model to development and mitigation of residual stresses and distortions in complex PBF components. Firstly, a 3D FE-based method is developed to predict the thermo-mechanical behavior of the NIST benchmark PBF manufactured Inconel 625 bridge structure [11]. A detailed validation of the FE-based model is presented by comparison against the published benchmark measurements. Residual stress and distortion predictions using the FE-based method are shown to agree closely with the measured data. The validated model is employed to investigate the influence of substrate

removal, and preheating and cooling rates on mitigating both residual stresses and distortions, as a guideline for selection of optimal manufacturing protocols and to demonstrate the effectiveness of the developed FE-based method.

2. Methodology

To improve computational efficiency, the widely-adopted sequentially coupled thermo-mechanical analysis of PBF process is used in this study [23, 31]. The transient heat transfer analysis is conducted first, for which the thermal loads are induced by the input laser during the printing process, as shown in Fig. 1, followed by a static mechanical analysis, where the calculated temperature field is imported to determine the residual stress caused by thermal expansion. The governing equations of both the thermal and mechanical analysis are briefly summarized in this section. More details of the thermal transfer and mechanical mechanisms can be found in [32].

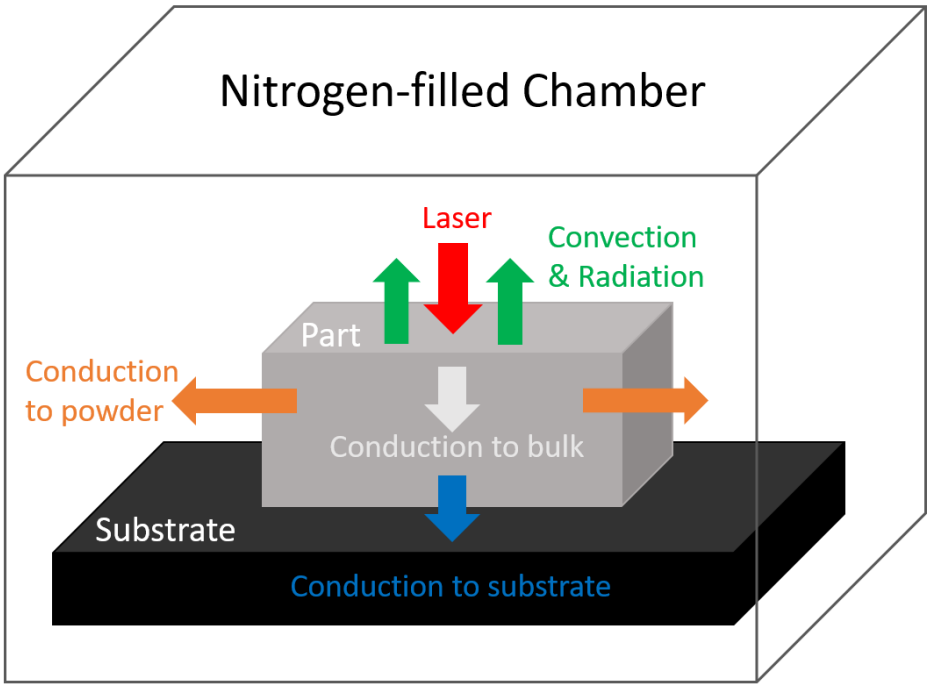

Fig. 1. Heat transfer mechanisms in the PBF process.

2.1 Governing equations

2.1.1 Thermal analysis

The governing equation of the thermal analysis is the heat conduction equation [33]:

$$\rho C_{\mathrm{p}} \frac{dT}{dt} + \nabla \cdot \mathbf{q} = Q + \dot{D}_{\mathrm{mech}} \tag{1}$$

where ρ is density ($\mathrm{kg/m^3}$), C_{p} is the temperature dependent specific heat ($\mathrm{J/(kgK)}$), T denotes temperature (K), t is time (s), $\mathbf{q}$ is heat flux vector, and Q is laser heat source, $\dot{D}_{\mathrm{mech}}$ is thermo-mechanical dissipation. The heat flux vector $\mathbf{q}$ due to conduction is given as follows:

$$\mathbf{q} = -k\nabla T \tag{2}$$

where k is the temperature dependent thermal conductivity ($\mathrm{W/(mK)}$). The heat loss due to heat convection can be formulated as:

$$q_{\mathrm{conv}} = h_{\mathrm{conv}}(T_{\mathrm{sur}} - T_{\mathrm{a}}) \tag{3}$$

where h_{conv} is heat transfer convection coefficient ($\mathrm{W/(m^2K)}$), taken as $18\ \mathrm{W/(m^2K)}$ during the printing process in this study [3], T_{sur} is surface temperature of the specimen (K), T_{a} is ambient temperature in build chamber (K). The heat loss due to radiation can be formulated as:

$$q_{\mathrm{rad}} = \varepsilon_{\mathrm{rad}}\sigma_{\mathrm{rad}}(T_{\mathrm{sur}}^4 - T_{\mathrm{a}}^4) \tag{4}$$

where $\varepsilon_{\mathrm{rad}}$ is the emissivity coefficient, and σ_{rad} is the Stefan–Boltzmann constant. Here the emissivity $\varepsilon_{\mathrm{rad}}$ and the Stefan-Boltzmann's constant σ_{rad} were set as 0.45 [34] and $5.669 \times 10^{-8}\ \mathrm{W/(m^2K^4)}$ [35], respectively. The laser heat source Q is modeled as a concentrated point heat source during the PBF process modelling [9, 36], which is expressed as:

$$Q = \frac{2\eta P}{abc\pi\sqrt{\pi}} \exp\left(-\frac{(x+vt)^2}{a} + \frac{y^2}{b} + \frac{z^2}{c}\right) \tag{5}$$

where P is the laser power, η is the absorptance, v is the velocity of moving laser heat source, a, b and c are the dimensions of the heat source along the x, y, and z axes, respectively.

2.1.2 Mechanical analysis

The governing equation of the mechanical analysis is the stress equilibrium equation [37], given as:

$$\nabla \cdot \boldsymbol{\sigma} = 0 \tag{6}$$

where $\boldsymbol{\sigma}$ is the stress tensor. The mechanical constitutive law for the elastic problem is defined as:

$$\boldsymbol{\sigma} = \boldsymbol{C} : \boldsymbol{\varepsilon_{\mathrm{e}}} = \boldsymbol{C} : (\boldsymbol{\varepsilon_{\mathrm{Total}}} - \boldsymbol{\varepsilon_{\mathrm{p}}} - \boldsymbol{\varepsilon_{\mathrm{T}}}) \tag{7}$$

where $\boldsymbol{C}$ is the stiffness tensor, $\boldsymbol{\varepsilon}_{\mathbf{Total}}$, $\boldsymbol{\varepsilon}_{\mathbf{e}}$, $\boldsymbol{\varepsilon}_{\mathbf{p}}$, $\boldsymbol{\varepsilon}_{\mathbf{T}}$ are the total, the elastic, the plastic and the thermal strain tensors, respectively. The thermal strain tensor driving the residual stress is calculated according to:

$$\boldsymbol{\varepsilon}_{\mathbf{T}} = \alpha \Delta T \boldsymbol{I} \tag{8}$$

where α is the temperature dependent thermal expansion coefficient (1/K), ΔT is the change in temperature (K) and $\boldsymbol{I}$ is identity tensor.

2.2 Finite element modelling of PBF process

Since the macro-scale residual stress and distortion cannot be predicted using the process-level modelling approach due to the prohibitively high computational cost, the component-level modelling approach is implemented here [23]. An overview of the PBF process modeling is illustrated in Fig. 2.

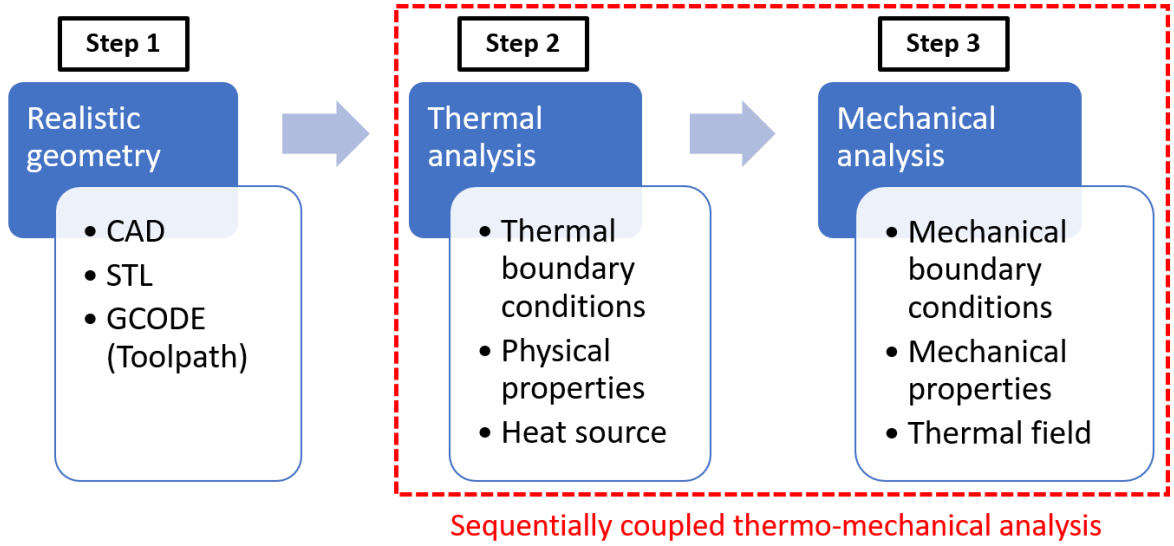

Fig. 2. Overview of the PBF process modelling: Step 1: Realistic geometry, Step 2: Thermal analysis, Step 3: Mechanical analysis.

The FE analysis is performed using Abaqus/CAE 2020 [38]. The built bridge-shaped geometry on a cuboid substrate modelled here using the 'Abaqus AM' method, of which more details can be found in our previous paper [30], is based on that experimentally examined by Phan et al. [11], as shown in Fig. 3. The dimensions of the printed component are 75 mm (L) × 5 mm (W) × 12.5 mm (H). The dimensions of the substrate are 81 mm (L) × 11 mm (W) × 12.7 mm (H). Fig. 3 (b) presents the FE model and mesh design. A detailed mesh convergence study was performed to achieve a judicious balance between required computational resource and

results accuracy (within 5% with respect to the maximum principal stress), as shown in Fig. 4. The element size of meshes P, Q and R (essentially uniform mesh distribution used in the bridge model) are 400 μm, 200 μm and 100 μm, respectively. The converged FE mesh Q consists of 486472 elements and 530988 nodes. The average element size in the bridge structure is 214 μm (L) × 200 μm (W) × 200 μm (H), i.e. layer scale-up factor of 10 (10 layers merged within one element layer). Similar mesh densities have been presented in Song et al. [9]. The ratio of element size to the characteristic length of component (12 mm) is 0.016. It should be noted that the mesh of the substrate is coarser (500 μm (L) × 500 μm (W) × 500 μm (H)), thus reducing computational cost whilst maintaining accuracy. The step increment is set as one time increment per build layer [9]. Eight-node linear heat transfer elements (DC3D8) are used for the heat transfer analysis, and eight-node linear elements with full integration (C3D8) are then applied for the mechanical analysis [9, 36].

Build direction is defined as the Z-direction for the PBF modelling, and the recoating is performed from right to left (along the opposite direction of the X-axis, see Fig. 5). The bottom surface of the substrate is fixed as shown in Fig. 5. The ambient temperature (T_a) in the build chamber and the predefined temperature (T_p) of the substrate are set the same as in the experiment, i.e. 313 K and 353 K, respectively [11]. In this study, the "cut" element set (see Fig. 5) between the bridge structure and the substrate is created to simulate the electric discharge machining (EDM) removal process, achieved by deactivating the "cut" element set after the whole bridge was built. The distortion of the bridge structure can be predicted and compared with the benchmark measurement.

(a)

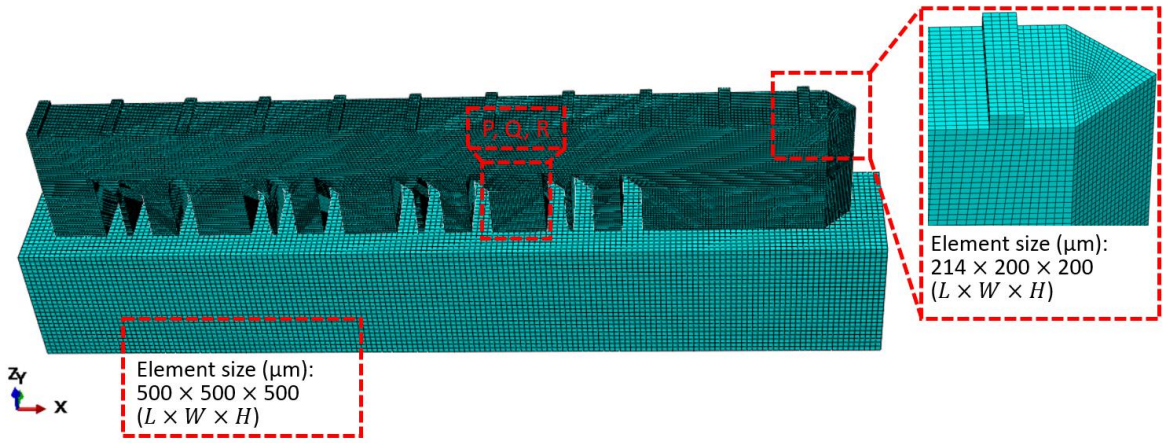

(b)

Fig. 3. Configurations of the PBF modelling: (a) Dimensions of bridge structure printed by Phan et al. [11], (b) FE model and mesh design.

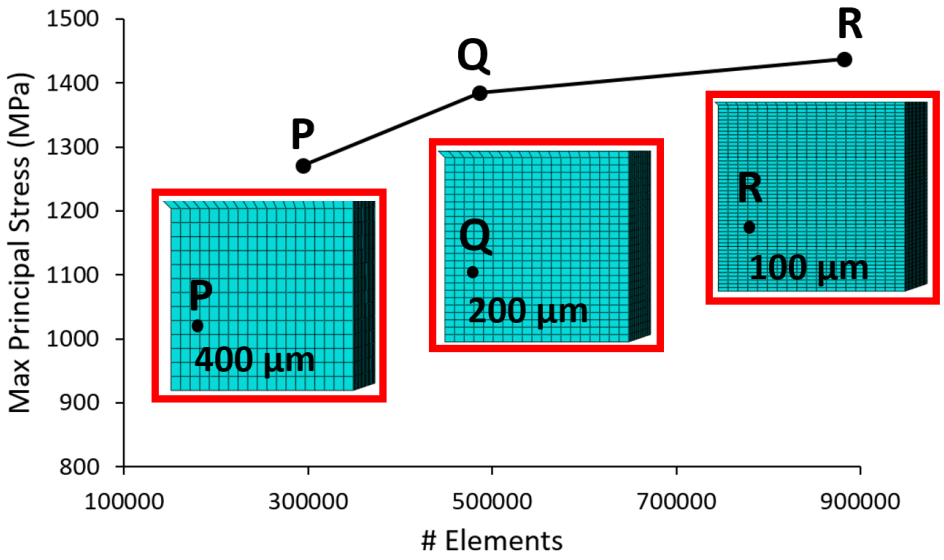

Fig. 4. Mesh convergency study (locations of P, Q and R see Fig. 3).

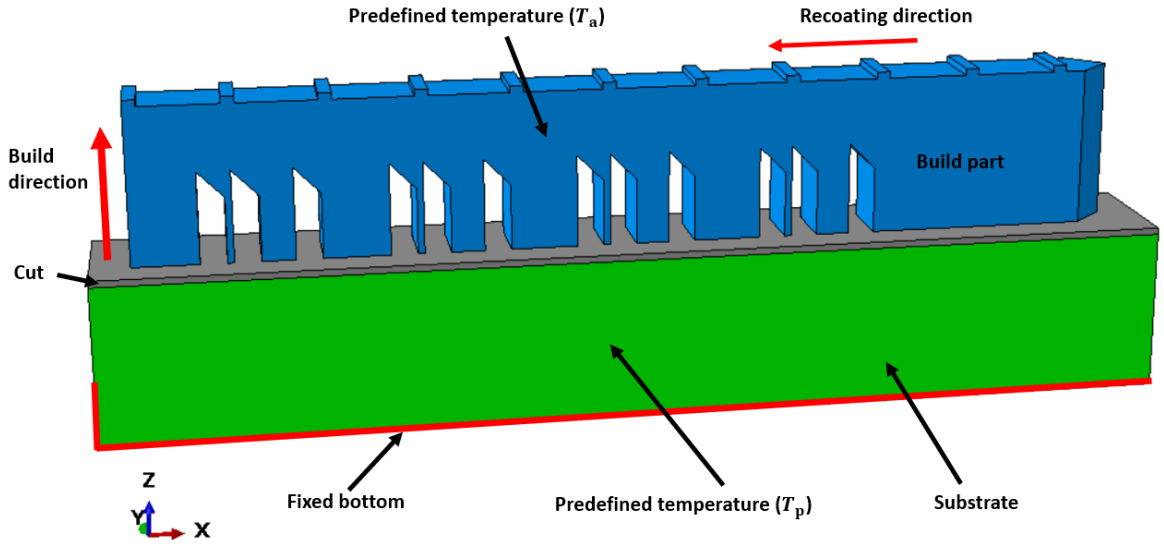

Fig. 5. Boundary conditions of the FE model.

2.3 Material properties and process parameters

The temperature-dependent material properties of Inconel 625 employed in this study are shown in Fig. 6, including thermal conductivity, specific heat, thermal expansion, Poisson's ratio, Young's modulus and yield stress [39, 40]. The material density is taken as a constant value of 8440 kg/m^3. The widely used elastic perfectly plastic (EPP) model is adopted to define the plasticity of Inconel 625 [41, 42]. The process parameters for the computational PBF modeling are summarized in Table 1, which are the same as the experiment conditions investigated here [11, 43]. The laser path employed in the PBF modelling is converted from G-code (i.e. combination of motion and action commands for the 3D printer) according to the scanning strategy (see Fig. 7, adapted from the NIST AM-Bench website [43]), including horizontal infill scans (parallel to the X-axis) and vertical scans (parallel to the Y-axis) for odd and even layers, respectively. The average layer time is 52 s during the printing of bridge legs.

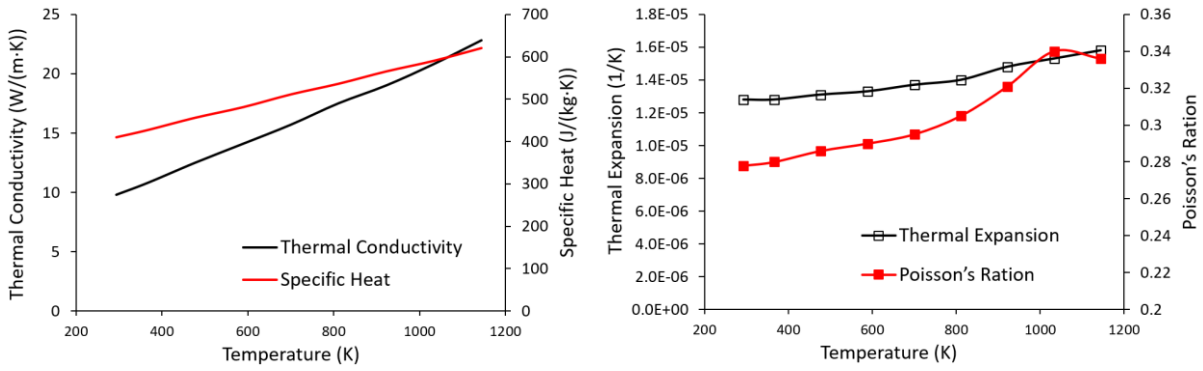

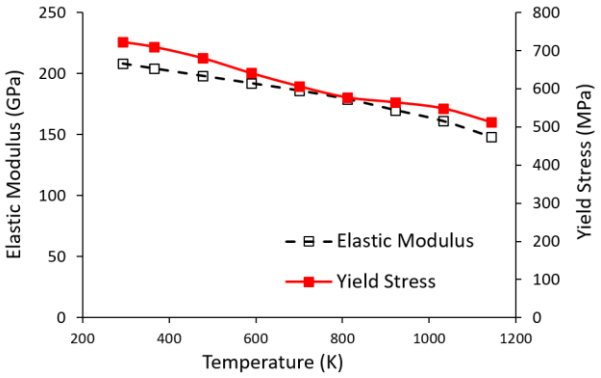

Fig. 6. Temperature-dependent material properties of Inconel 625 [39, 40].

Table 1. Process parameters applied in the PBF modelling.

Symbol	Parameters	Value
η	Absorption coefficient	0.45
P_c	Contour laser power (W)	100
v_c	Contour scanning speed (mm/s)	900
P_i	Infill laser power (W)	195
v_i	Infill scanning speed (mm/s)	800
d_s	Laser spot diameter (μm)	50
L	Layer thickness (μm)	20
H	Hatch spacing (μm)	100

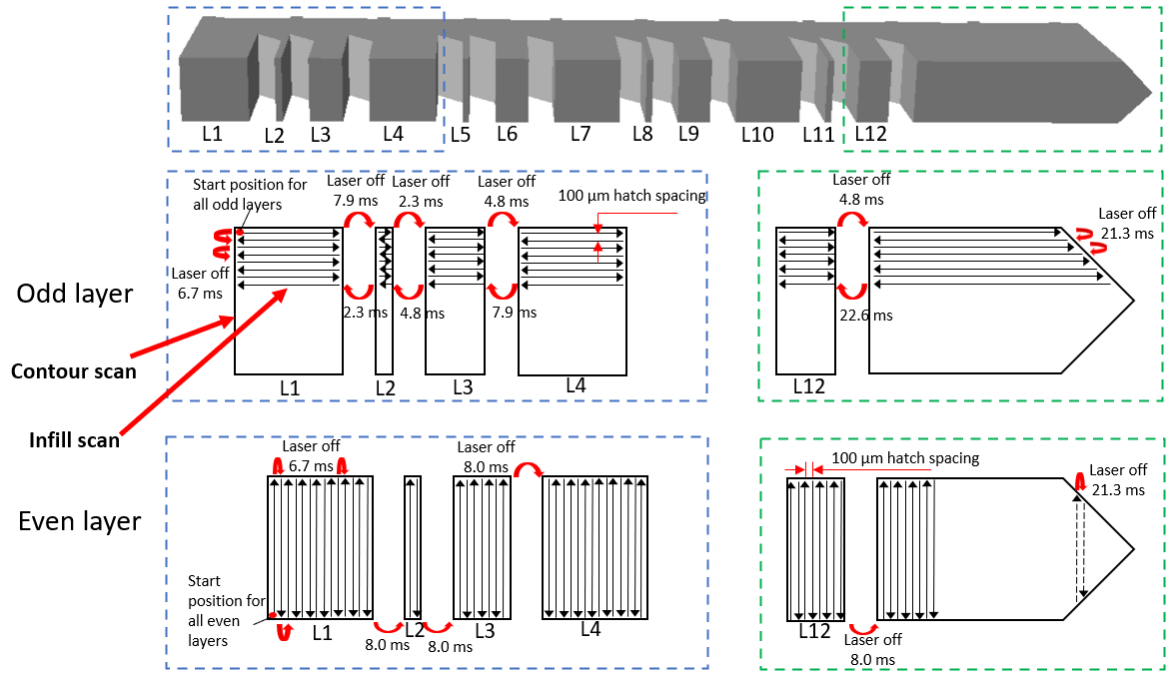

Fig. 7. Scanning strategy, adapted from NIST AM-Bench website [43].

3. Results

3. 1 Validation of thermo-mechanical FE model

3.1.1 Residual strain analysis

To validate the performance of the present FE-based component-level model, prediction of residual strains, residual stresses and distortions in Inconel 625 bridge is compared with the test data of Phan et al. [11]. First, the residual strain in the middle cross section of the manufactured bridge structure is predicted and compared to the experimental measurements (before substrate removal). Figs. 8 (a), (c) and (e) shows the predicted distributions of residual strains ε_{xx}, ε_{zz} and ε_{xz}, respectively. The corresponding experimental measurements are shown in Figs. 8 (b), (d) and (f). It is clear that all three predicted residual strain distributions are in reasonable agreement with the benchmark measurements from Phan et al. [11], in terms of both magnitude and distribution. Specifically, both FE prediction and XRD measurement of the residual strain ε_{xx} (see Figs. 8 (a) and (b)) are mostly tensile across the main body of the bridge structure, while the compressive strains are mainly on the bridge legs. The maximum tensile strains are close to the top and bottom sides of the bridge. The predicted residual strain ε_{zz} shown in Fig. 8 (c) is in reasonable agreement with the experimental measured residual strain ε_{zz} (see Fig. 8 (d)), with mostly compressive strain through the main body and tensile strain on the bridge legs, which is almost a reverse image to that in the X direction. Similar

agreement is also obtained for the shear strain ε_{xz} (see Figs. 8 (e) and (f)).

In order to make more specific quantitative comparisons, three horizontal paths for comparison between the predicted and XRD measured residual strain ε_{zz} are defined in Fig. 9 (a). The comparison of the residual strain ε_{zz} at the three different heights are: near the top surface of the bridge structure (Z = 11.25 mm, see Fig. 9 (b)), near the middle of the top solid section (Z = 9.75 mm, see Fig. 9 (c)), and through the legs of the bridge structure (Z = 2.25 mm, see Fig. 9 (d)). Overall, good agreement is obtained between the predictions and experimental measurements. A preliminary study is conducted to optimize the use of multiple cores at each step to minimize the total computational time required for analysis using the component-level approach. For our case, running using processor with 8 cores, the total runtime for this model is about 9.5 hours for thermal analysis and around 43 h for the mechanical analysis.

(a)

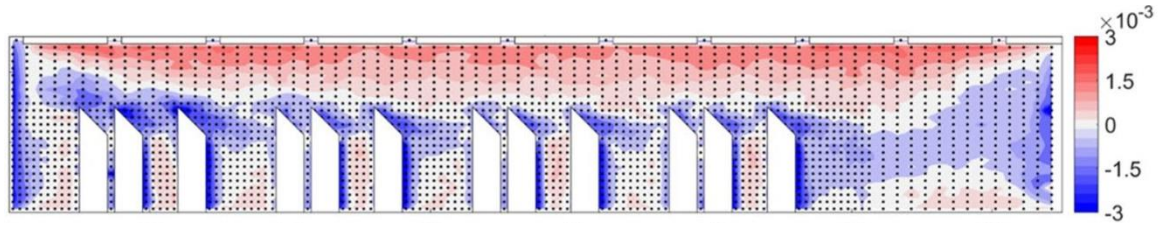

(b)

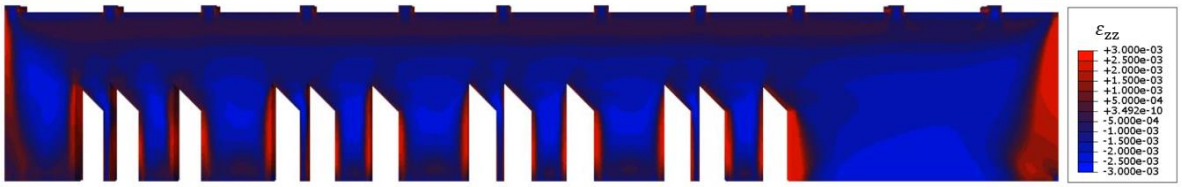

(c)

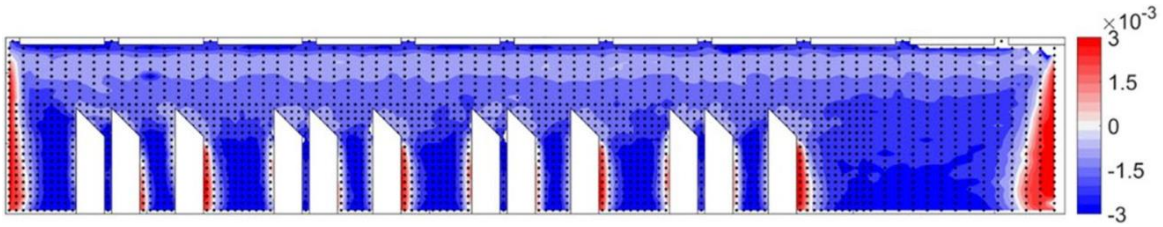

(d)

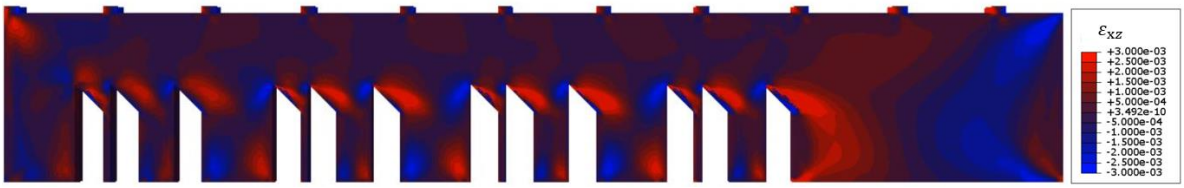

(e)

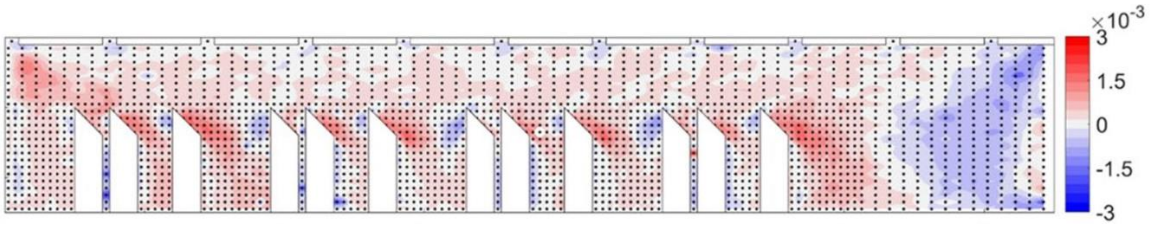

(f)

Fig. 8. The comparison of predicted and XRD measured [11] residual strain in the middle cross section of the bridge structure (before substrate removal): (a) predicted residual strain ε_{xx}, (b) XRD measured residual strain ε_{xx}, (c) predicted residual strain ε_{zz}, (d) XRD measured residual strain ε_{zz}, (e) predicted residual strain ε_{xz}, (f) XRD measured residual strain ε_{xz}.

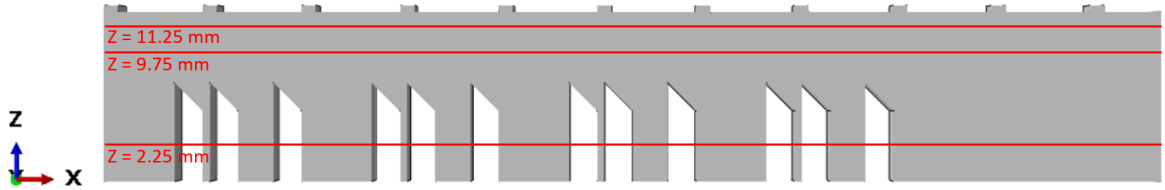

(a)

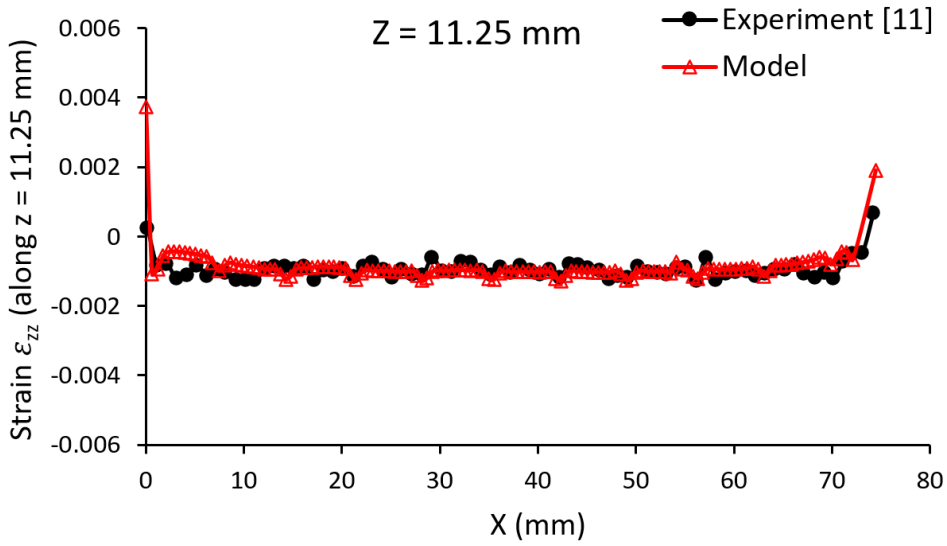

(b)

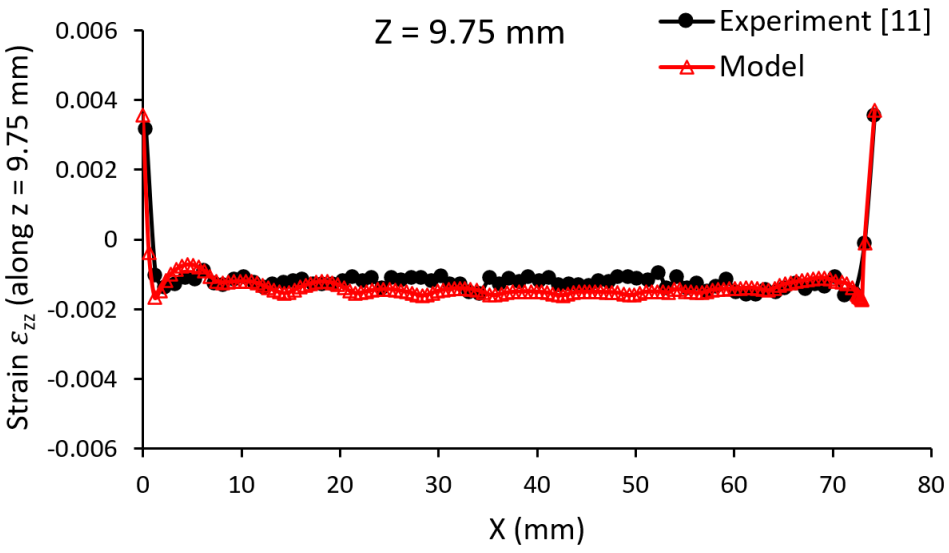

(c)

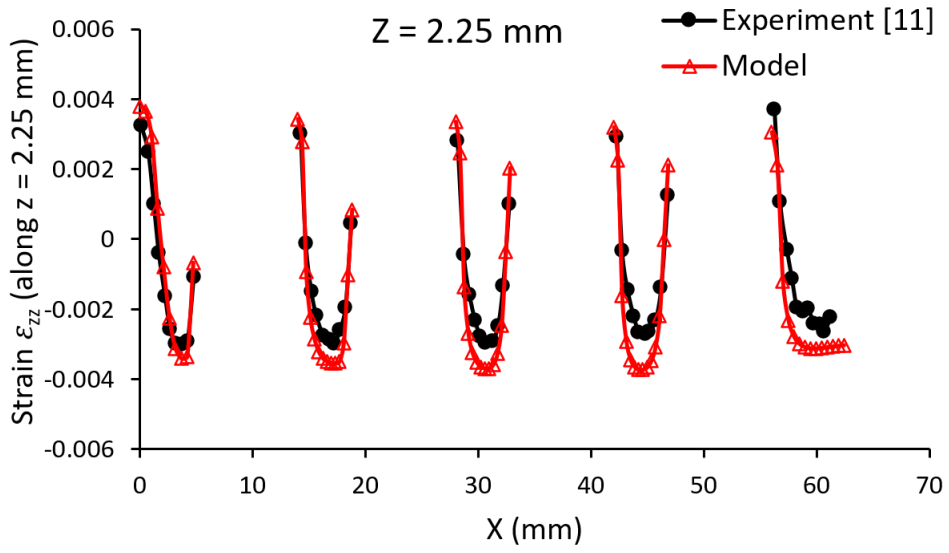

(d)

Fig. 9. The comparison of predictions and XRD measurements [11] of residual strain ε_{zz} along different paths: (a) locations of the paths, (b) path of Z = 11.25 mm, (c) path of Z = 9.75 mm, (d) path of Z = 2.25 mm.

3.1.2 Residual stress analysis

Fig. 10 shows the comparison of FE predicted and contour method measured residual stress σ_{xx} on the plane at the 7th leg (marked as 'L7', located at X = 31 mm, see Fig. 10 (a)). The predicted residual stress in the X direction (Fig. 10 (b)) is in close agreement with the experimental measurement (Fig. 10 (c)). Fig. 11 shows the comparison of FE predicted, contour method and neutron diffraction measured residual stress σ_{xx} along the vertical line at the center of the L7 plane. Both the trend and values from the FE prediction and benchmark measurements

show reasonable agreement except near the top and bottom of the bridge structure.

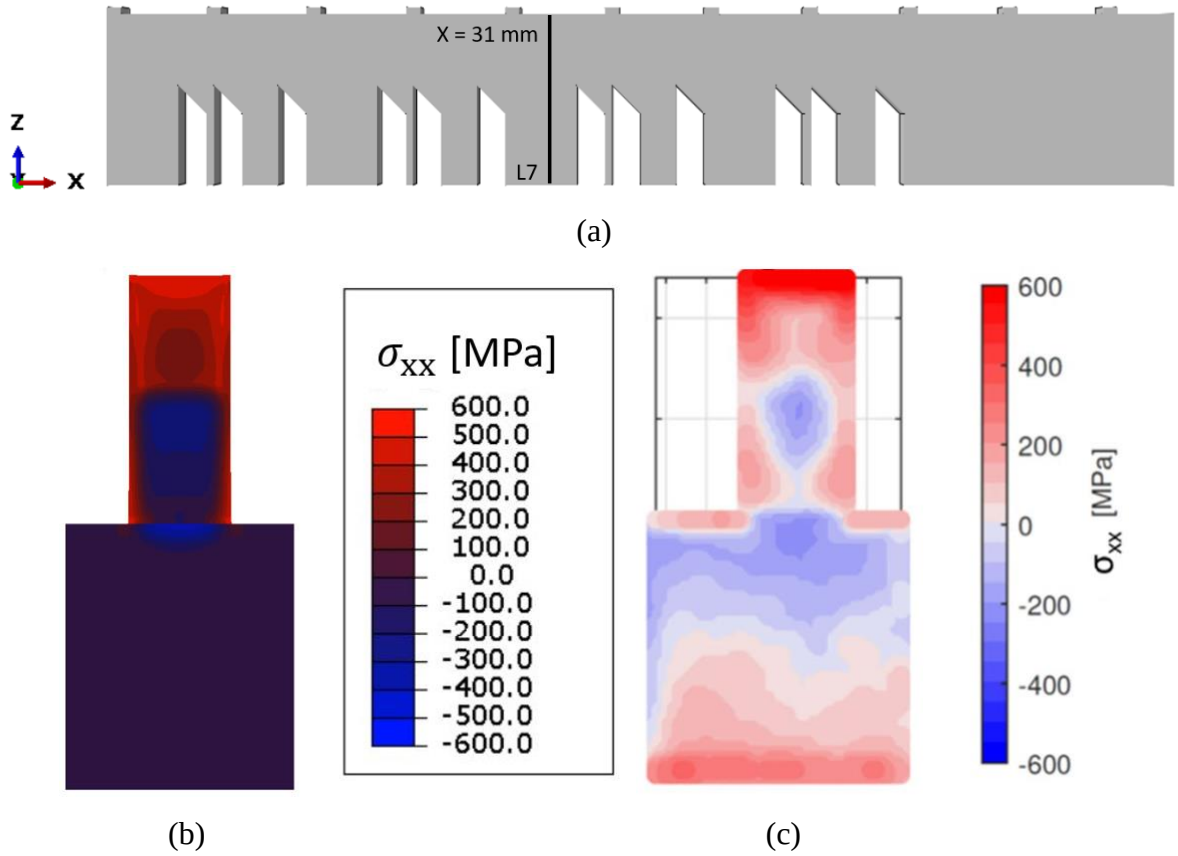

Fig. 10. The comparison of FE predicted and contour method measured [11] residual stress σ_{xx} on the plane at the 7th leg (marked as 'L7'): (a) location of the 'L7' plane (at X = 31 mm), (b) FE predicted residual stress σ_{xx}, (c) measured residual stress σ_{xx} using the contour method.

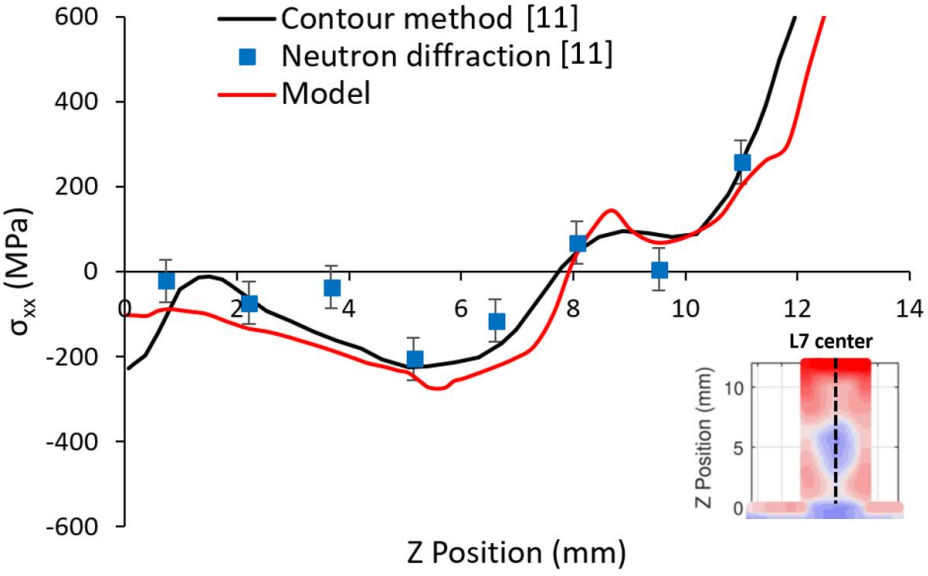

Fig. 11. Comparison of FE predicted and experimental measured [11] residual stress distributions

along the vertical line at the center of the L7 plane.

3.1.3 Distortion analysis

Distortion of the bridge after the EDM removal process is simulated to investigate the ability of the present model to predict the direction and magnitude of distortion. Fig. 12 shows the comparison of the distortion calculated by the FE model with CMM measurements [11]. The measurement points are indicated by the solid black dots on the ridges along the top of the bridge. The Z direction displacement is calculated as the difference between the measurement before and after the twelve legs of the bridge been separated from the substrate. Fig. 13 shows the corresponding bridge distortion after EDM by Phan et al. [11]. The predicted distortion and the experimental result show the same upward distortion (in the build direction, see Fig. 5), and the predicted maximum Z displacement is 1.1 mm, which is in close agreement with the experimental measurement of 1.27 mm.

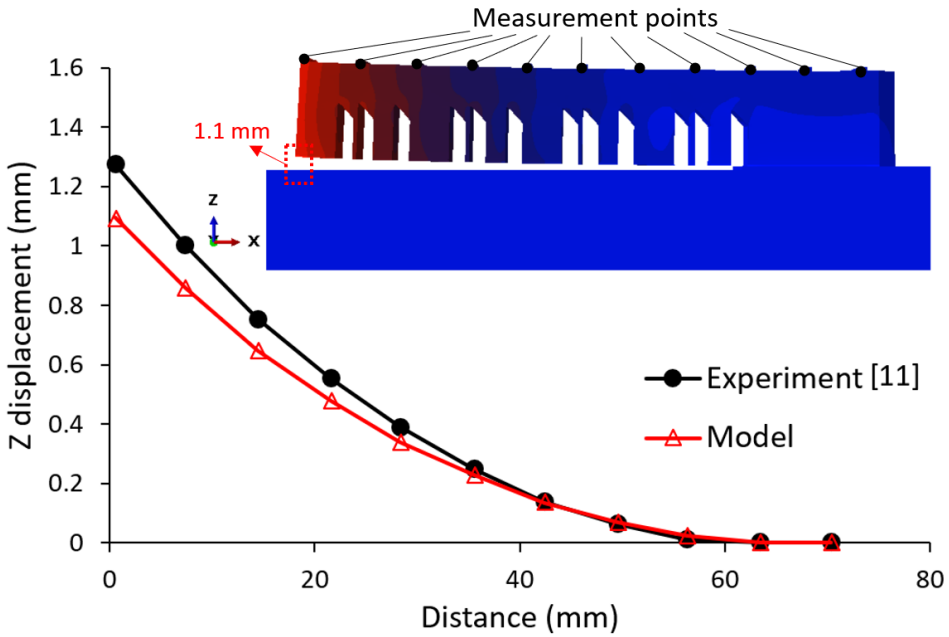

Fig. 12. Comparison of present FE predicted distortion with experimental measurement [11].

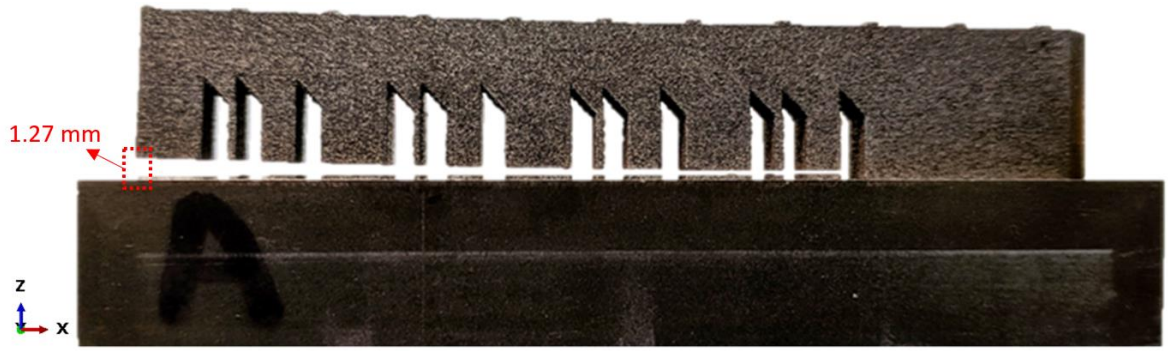

Fig. 13. Macrograph of bridge distortion after EDM process, adapted from Phan et al. [11].

3. 2 The effect of substrate removal on the residual stress and distortion

3. 2.1 Residual stress

Fig. 14 shows the predicted contours of the maximum principal stress of the bridge before and after removal of the substrate. Before cutting off from the substrate, the maximum principal stress (1385 MPa) is found at the bottom of the bridge (region connected to the substrate, see Fig. 14 (a)). After cutting off from the substrate, the maximum principal stress decreases to 1049 MPa, and the location of the stress concentration changes to the side of the bridge legs (see Fig. 14 (b)). Ahmad et al. [44] evaluated the residual stress in SLM Inconel 718 samples using the contour method, showing that detrimentally-high tensile residual stress occurred at and near the side surfaces of the AM Inconel alloys samples. Fig. 15 shows the effect of cutting on the residual maximum principal and normal (Cartesian) stress component distributions along two paths, i.e. L1 (along top surface, x-direction) and L2 (through height, z-direction), as shown in Fig. 14. In general, it can be found that the most significant effect of cutting occurs closest to the plane of cutting, i.e. for low values of Z, as shown in Figs. 15 (b), 15 (d), 15 (f) and 15 (h). The σ_{xx} (Mode I type) residual stress along L1 is significantly reduced from tensile (detrimental), about 300 MPa, to compressive (beneficial), about 100 MPa, but the σ_{yy} and σ_{zz} components are negligibly affected along this line. The dominant residual stress before and after cutting is σ_{zz} and it is highest along L1 (top surface) and only negligibly affected there by cutting; through the height (L2), σ_{zz} is significantly reduced from a uniformly high tensile value to a linearly reducing value, reaching almost zero at the bottom surface (cutting plane); in contrast, σ_{xx} and σ_{yy} are negligibly affected except very close to the bottom surface (cutting plane), where the values also reduce to almost zero. Although the residual σ_{zz} stress along the top surface is not typically Mode I, since it is not parallel to the free surface, it is conceivable that these residual tensile stresses could interact with residual porosity and lead to sub-surface

cracking in fatigue, or rolling contact fatigue, leading to delamination effects for example.

The maximum residual stress values for σ_{xx}, σ_{yy}, σ_{zz} and maximum principal stress, of the bridge before and after cutting off from the substrate, are summarized in Fig. 16. Removal of the substrate results in decrease in all residual stress components. The maximum decrease is 335.8 MPa, for maximum principal stress, while the minimum decrease in σ_{yy} is only 10.2 MPa.

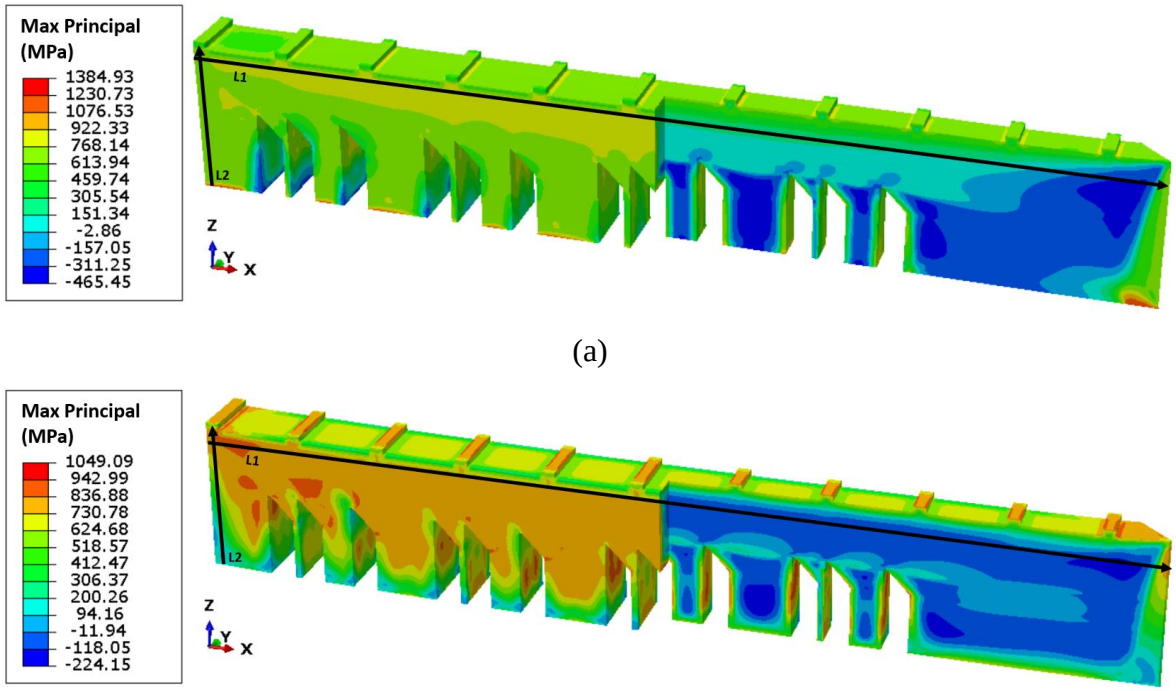

Fig. 14. The residual maximum principal stress of the bridge: (a) before cutting off from the substrate, (b) after cutting off from the substrate.

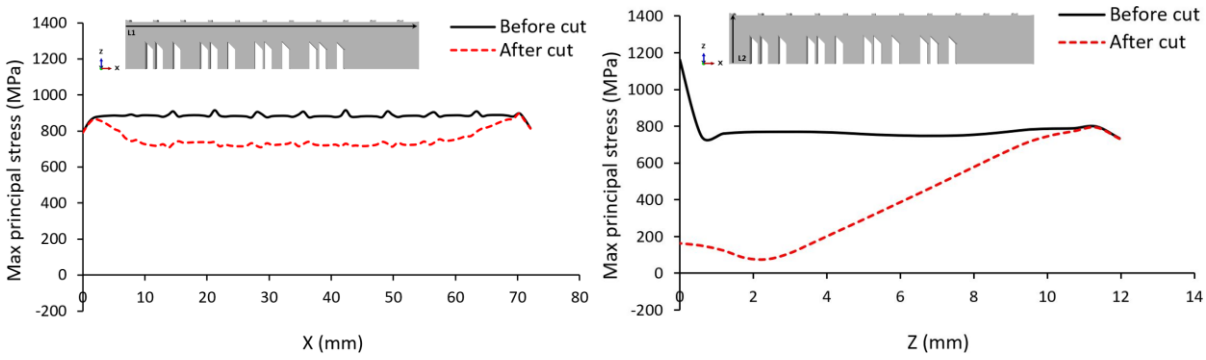

(a) Maximum principal stress along top surface (L1) (b) Maximum principal stress through height (L2)

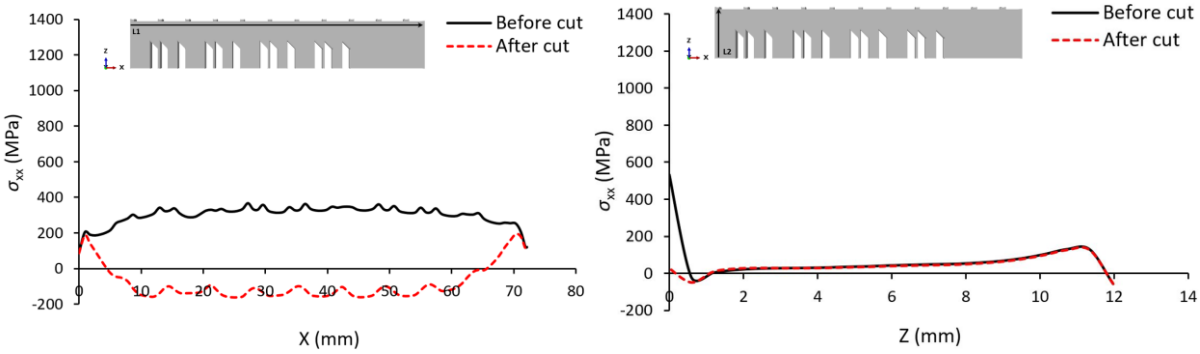

(c) σ_{xx} along top surface (L1) (d) σ_{xx} through height (L2)

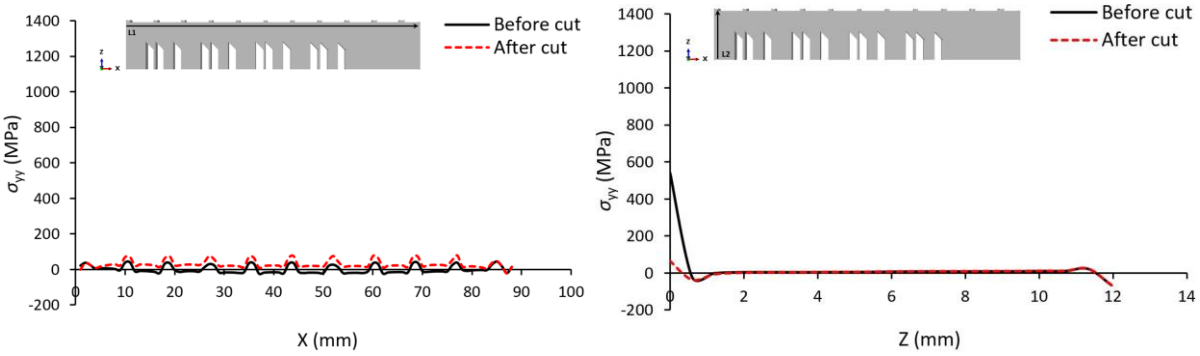

(e) σ_{yy} along top surface (L1) (f) σ_{yy} through height (L2)

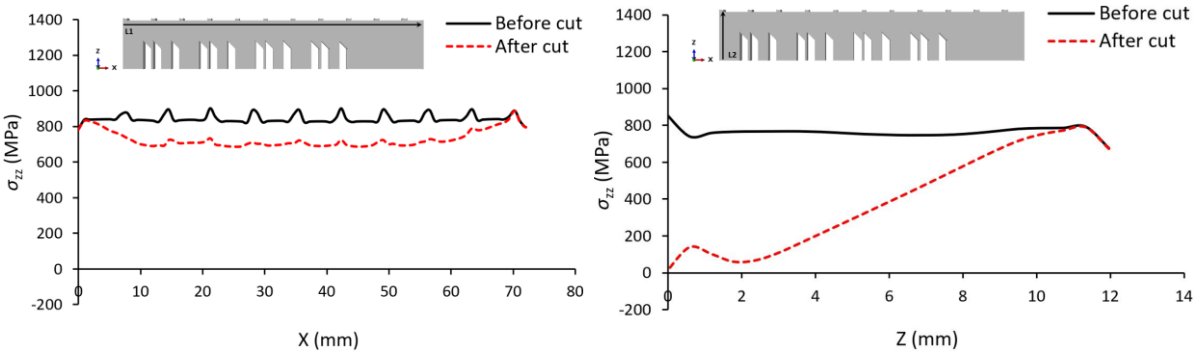

(g) σ_{zz} along top surface (L1) (h) σ_{zz} through height (L2)

Fig. 15. Effect of cutting on residual stress distributions of bridge for maximum principal stress and normal (Cartesian) stress components along top surface (L1) and through height (L2): (a) maximum principal stress along top surface (L1), (b) maximum principal stress through height (L2), (c) σ_{xx} along top surface (L1), (d) σ_{xx} through height (L2), (e) σ_{yy} along top surface (L1), (f) σ_{yy} through height (L2), (g) σ_{zz} along top surface (L1), (h) σ_{zz} through height (L2).

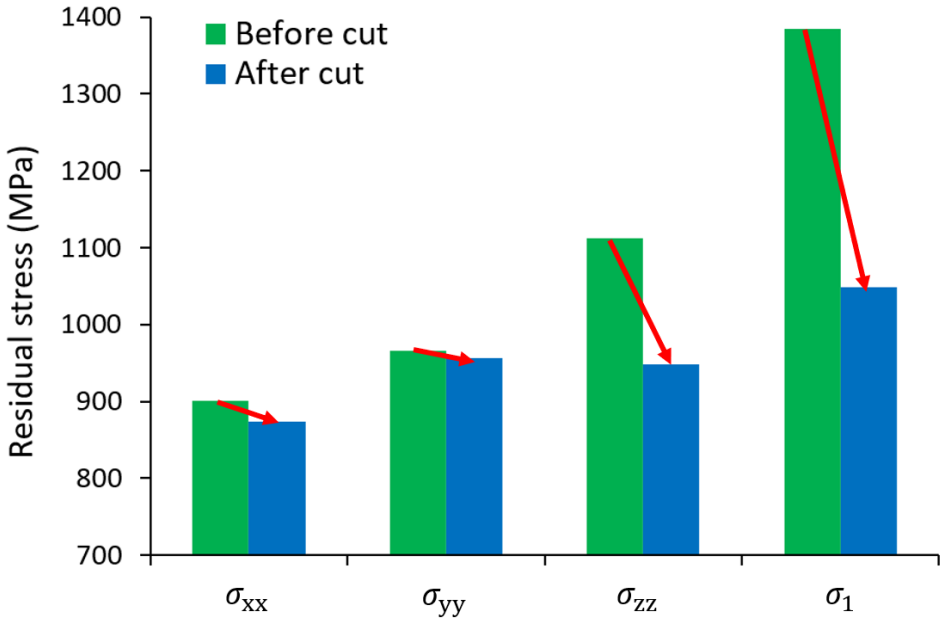

Fig. 16. Maximum residual stress values for σ_{xx}, σ_{yy}, σ_{zz} and maximum principal stress before and after cutting off from the substrate.

3. 2.2 Z direction distortion

The distortion of the bridge in the Z (vertical) direction after fully cutting off from the substrate is shown in Fig. 17, which is different from that of the bridge with twelve legs separated from the substrate (see Figs. 12 and 13). This is attributes to the lack of constraints from the substrate (after fully cutting off) and thus the bridge has more freedom to deform in both sides.

Fig. 17. FE-predicted component distortion after fully cutting off from the substrate.

3. 3 The effect of preheating and cooling rate on the residual stress and distortion

Fig. 18 shows the comparison of predicted maximum principal stress distributions along path ‘L1’ under different preheating conditions before and after cutting off from the substrate.

The results show that increasing preheating temperature and ambient temperature can effectively mitigate the residual stress. When the preheating temperature is increased to 973 K, with the ambient temperature fixed at 313 K, the maximum principal stress along path 'L1' on the surface of the bridge decreases more than half (from 915.7 MPa to 429.9 MPa) before cutting off from the substrate (see Fig. 18 (a)). When the ambient temperature is increased to 673 K, the residual maximum principal stress is less than 200 MPa. The same analysis applies after cutting off the substrate, as shown in Fig. 18 (b).

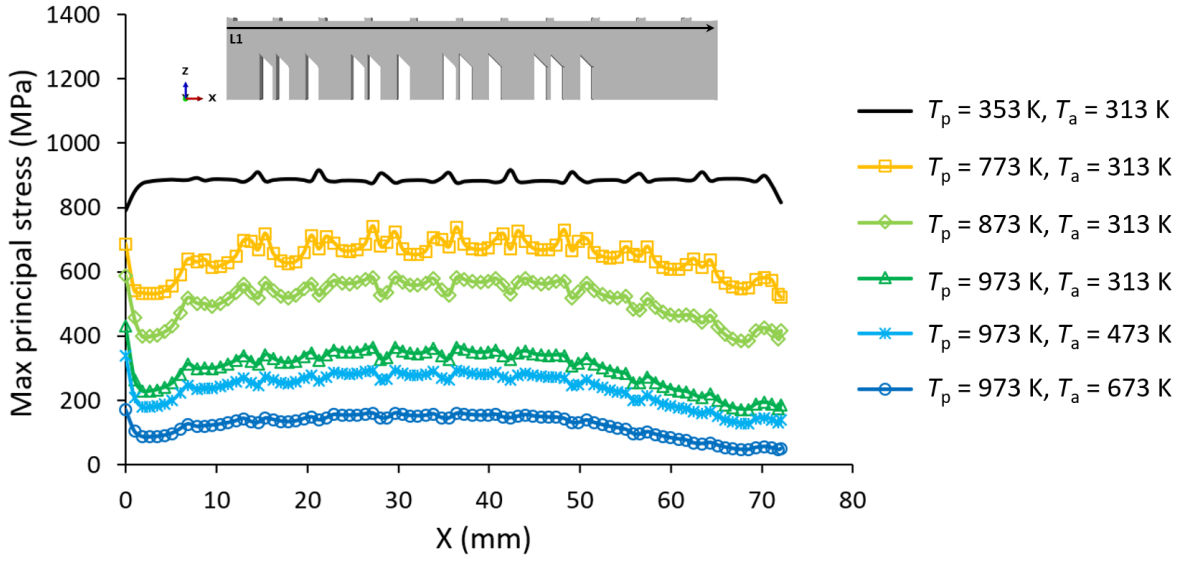

(a)

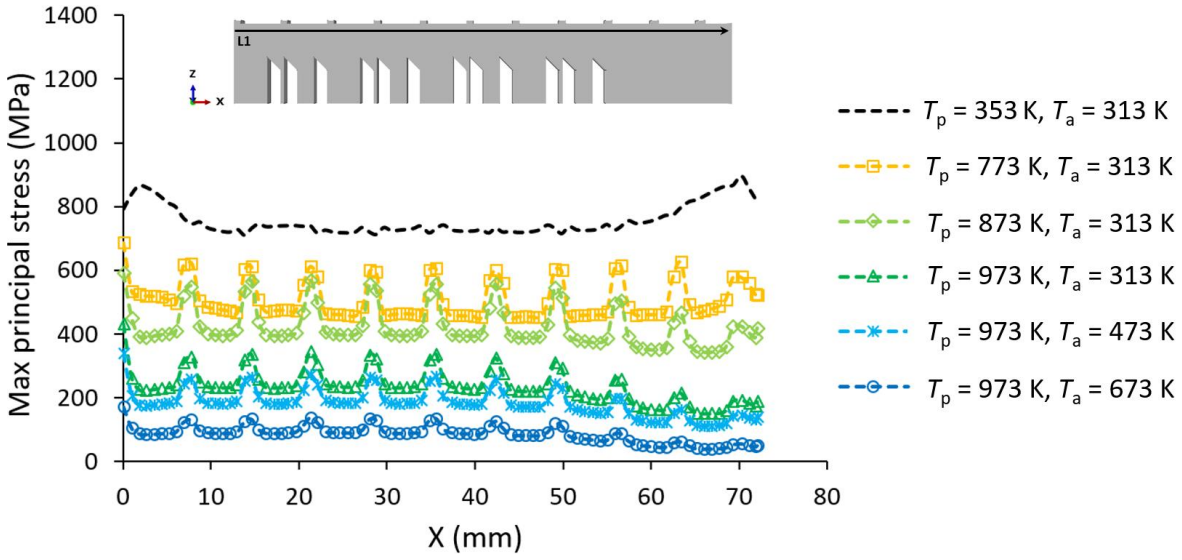

(b)

Fig. 18. The comparison of predicted maximum principal stress distributions along path 'L1' under different preheating conditions: (a) before cutting off from the substrate, (b) after cutting

off from the substrate.

Fig. 19 shows the influence of preheating conditions on the distortion of the bridge after cutting off from the substrate. Increasing the preheating temperature reduces the distortion. In particular, the maximum Z displacement of the bridge does not exceed 0.05 mm when the temperature of the substrate is increased to 973 K (condition 4). When the ambient temperature reaches 673 K, the distortion of the bridge almost vanishes (0.01 mm).

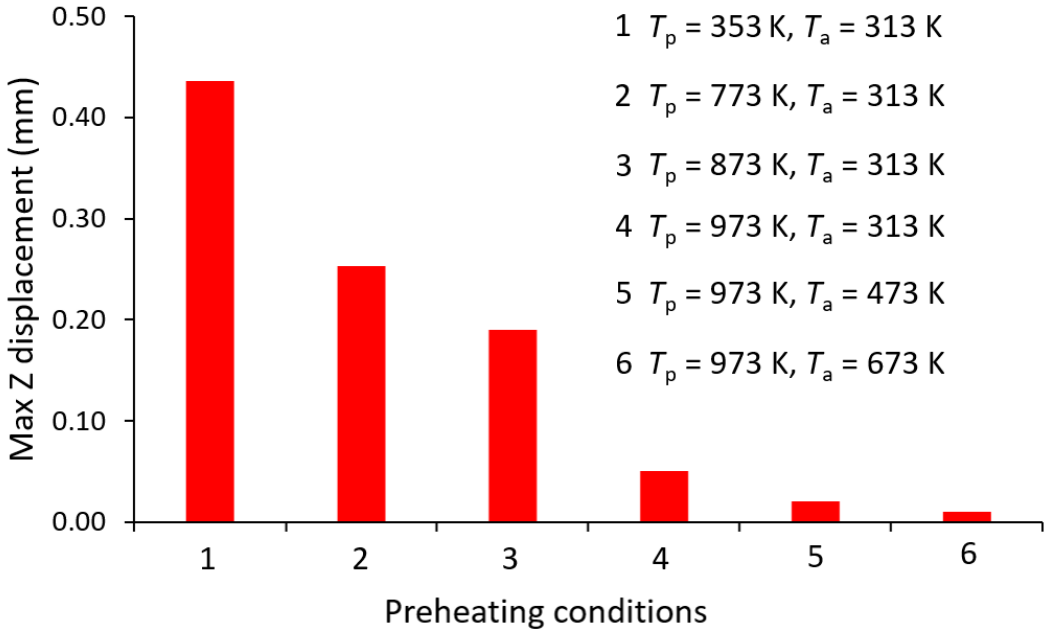

Fig. 19. The comparison of predicted maximum Z displacement of the bridge after cutting off from the substrate under different preheating conditions.

4. Discussion

A key objective of the present study is the prediction of residual stresses and distortions induced by the PBF process. A specific challenge is to study the complex geometries at the component-level while preserving the accuracy and efficiency of the prediction. In this study, the FE-based 'Abaqus AM' method is used for simulating the PBF process of large-scale complex geometry, including investigation on effects of substrate removal and preheating on mitigation of residual stresses and distortions, as most of existing component-level modelling approaches ignore many of the important influencing factors for reduction of computational time, for example, the effect of scan strategy is not included in the pragmatic part scale model [23]. In the present model, the printing related information, including laser power, velocity, hatch

spacing, scanning strategy and laser off time (see Fig. 7), are directly converted from the actual data (G-code) with no loss of modelling accuracy.

In contrast to the DED process, the layer thickness is relatively small with a larger number of total layers and the process parameters are usually unchanged throughout the PBF process [45, 46]. The model size as well as the number of layers within the model are restricted by the computational expense [47]. Hence, it is important to reduce the computational cost to make the use of FE-based AM modelling method practical for industry applications. Different modelling strategies have been proposed to reduce the computational cost and the output file size, such as layer agglomeration approach (also referred as 'layer lumping approach'), in which many layers are combined into one larger computational layer (viz. use one element to represent multiple layers) [48]. Thus, choice of appropriate element size is essential for a judicious balance between result accuracy and computational time. Therefore, the mesh height of 0.2 mm of the bridge component (of 10 physically printed layers) is chosen in the present study (see Figs. 3 and 4). In the thermal analysis presented here, the concentrated heat source model is implemented via the built-in point toolpath-mesh intersection module to describe the moving heat flux during the PBF process, due to the relatively large element size compared to the laser beam radius [38]. The moving heat source is calculated based on the actual laser path to capture the spatial and temporal representation of the energy distribution accurately. Song et al. [9] have presented a validation study of the point toolpath-mesh intersection approach for a coarse mesh via comparison against the generally-accepted Goldak-type approach with fine mesh using similar step increment, highlighting the deformations in the PBF process can be captured by the point heating approach with coarse mesh. Nyce et al. [36] have also performed comparison of temperature distributions between the concentrated point heat source model and the Goldak heat source model. Very similar temperature profiles were obtained for the two heating models.

The mechanical response (residual stresses and distortions) is calculated from the sequentially coupled thermo-mechanical FE analysis in this study. This is valid since the mechanical responses resulting from rapid thermal evolution having very little effect on the associated thermal fields or the phase transformation behaviour, as the laser energy is much larger than the strain energy in the built part [49]. Yang et al. [42] and Huang et al. [50] have compared the sequentially coupled thermal-mechanical analysis to the fully coupled analysis: both cases show negligible difference between the two kinds of analysis. The reasonable agreement between the predicted residual strain and stress contours and experimental measurements (see

Figs. 8 and 10) indicate that a layer scale-up factor of 10 (Fig. 3) would result in an acceptable prediction accuracy. In other words, it is acceptable to use the layer lumping approach with point heating source. The material expands when the laser beam starts melting the metal powder, which will be limited as the surrounding material is colder. The temperature of the new melted top layer is always higher than the underlying layer during the heating process. During the cooling process, the contraction in the warmer upper layer is greater than the colder underlying layer. However, the contraction is inhibited due to the connection of both layers, causing tensile and compressive residual stress in the upper and underlying layer, respectively [10]. Large tensile residual stress is produced in the upper side (see Fig. 10) after the printing process, lots of tensile residual stresses are released and the built bridge component stays at a concave shaped distortion after cutting off the twelve legs (see Figs. 12 and 13) or the whole substrate (see Fig. 17). It is found that the model predicts the same upward distortion direction as the experiment, but slightly under-predicts the maximum distortion magnitude (viz. 1.1 mm, as compared to 1.27 mm, see Fig. 12). Similar under-prediction was obtained by Papadakis et al. [51] on an Inconel 718 cantilever using the layer-by-layer modelling method (predicted deformation of 0.6 mm compared to experimental measured deformation of 0.8 mm) and by Li et al. [37] on the AlSi10Mg cantilever using the temperature-thread multiscale FE method (predicted maximum distortion was 1.5 mm while the measured data was 2.1 mm). One possible reason could be that the EPP material constitutive model is used in the present study instead of considering the complex strain hardening effects and residual stresses induced by phase transformation during the PBF process [52]. Another possible reason could be that the wire EDM process would generate extra residual stress to the bridge since EDM is a thermal process [53], which could make the final distortion larger (see Fig. 12). These two aspects could be included in future work. Although the present component-level modelling method uses some simplifications (i.e. coarse mesh and large step increment), which affect the predicted thermal history and cooling rate [30], it enables computationally-efficient component-level analysis of the distribution of residual stresses in the printed components without sacrificing accuracy.

A key additional novel contribution of this work is using the validated model to investigate the effects of preheating and cooling rate on the residual stresses and distortions of a complex 3D component. Mirkoohi et al. [54] have proposed a physics-based analytical model to investigate the effect of substrate temperature on residual stress in PBF of Inconel 718, showing that preheating the substrate reduces residual stress in AM parts due to the reduction of temperature gradients, which has been validated against XRD measurements on PBF Inconel

718 samples. The effectiveness of reducing residual stresses by preheating, however, needs to be proven for a complex 3D geometry. Hence, different preheating conditions (preheating temperatures and cooling rates) are examined in this study. The present work successfully reveals and captures the beneficial effect of preheating on the Inconel 625 bridge structure. Significant influences of preheating and cooling rate on residual stress are also predicted by Cao et al. [55] and Lu et al. [56]. Vrancken et al. [57] experimentally measured the residual stress of Ti-6Al-4V parts produced by SLM under different preheating temperatures (100 ^{o}C, 200 ^{o}C, 300 ^{o}C, 400 ^{o}C) using XRD, demonstrating benefits of preheating the substrate, as the residual stress was significantly reduced from 628 MPa with no preheating, to 313 MPa under 400 ^{o}C preheating. Through investigation on the effects of different preheating temperature on SLM Inconel 738 by numerical simulation and experimental analysis, Wang et al. [58] found that the temperature gradients obviously reduced with increased preheating temperature: the maximum drop in temperature gradients was around 25% when the preheating was increased from 200 ^{o}C to 600 ^{o}C. Lower temperature gradients and cooling rates make the phase change process more stable, which reduces the residual stresses. Based on the results shown in Figs. 18 and 19, an appropriate preheating condition should be selected for mitigating the residual stress and distortion of AM components, particularly the tensile residual stresses, which are detrimental to fatigue resistance [59]. Hua et al. [60] investigated the influence of residual stress on fatigue performance of Inconel 718, experimentally showing that the fatigue life increased by 83.6% with the mitigation of residual stress by 17.9%.

Recently, Yang et al. [20, 61] have presented a process-structure model and a structure-property model, successfully predicting the microstructure attributes (e.g. columnar-equiaxed morphology, phase fractions and lath width) and stress-strain responses (including yield stress, ultimate tensile strength, uniform elongation and flow stress). Zhang et al. [62] introduced an FE-based generic metallurgical phase transformation framework, allowing the user to define and to model phase transformations in an alloy during AM process. In future work, it is planned to extend the current model to include the metallurgical phase transformation model, the process-structure model and the structure-property model to provide a pragmatic model to address the process-structure-property-performance (PSPP) relationships and optimize the AM process for manufacturing real-scale components with improved mechanical performance (e.g. tensile and fatigue) for industrial applications.

5. Conclusions

This paper presents an efficient and accurate component-level finite element thermo-mechanical model for predicting residual stress and distortion in the PBF manufactured complex Inconel 625 bridge. The developed model is verified and validated through mesh sensitivity studies and detailed comparisons against NIST benchmark measurements. The validated model is used to investigate the effects of substrate removal and preheating conditions on residual stresses and distortions. The key conclusions are:

- Comparison to detailed measurements from Phan et al. [11] has shown that the component-level finite element process model accurately predicts transient development of residual strains, stresses and distortions.
- It is shown that significant improvement in computational efficiency is achieved with minimal sacrifice in accuracy by simulating multiple printing layers (layer scale-up).
- The model shows that removal of substrate gives a significant beneficial reduction of residual stress of 335.8 MPa (24.2%) and distortion of the Inconel 625 bridge component.
- The model shows that increasing preheating temperature and decreasing cooling rate can significantly mitigate the residual stresses and distortions, by 81% and 98%, respectively.
- The present study offers practical guidelines on selection of optimal PBF protocols and a practical method for integrating finite element based PBF modelling into industry design and manufacturing systems.

Declaration of Competing Interest

The authors declare that they have no known competing financial interests or personal relationships that could have appeared to influence the work reported in this paper.

Acknowledgements

This publication has emanated from research conducted with the financial support of Science Foundation Ireland under Grant number SFI/16/RC/3872. For the purpose of Open Access, the author has applied a CC BY public copyright licence to any Author Accepted Manuscript version arising from this submission.

References

1. Frazier WE. Metal additive manufacturing: a review. *Journal of Materials Engineering and performance*. 2014; 23: 1917-28.
2. Gatsos T, Elsayed KA, Zhai Y, Lados DA. Review on Computational Modeling of Process–Microstructure–Property Relationships in Metal Additive Manufacturing. *JOM*. 2020; 72: 403-19.
3. Denlinger ER, Michaleris P. Effect of stress relaxation on distortion in additive manufacturing process modeling. *Additive Manufacturing*. 2016; 12: 51-9.
4. Bartlett JL, Li X. An overview of residual stresses in metal powder bed fusion. *Additive Manufacturing*. 2019; 27: 131-49.
5. Chen S-g, Gao H-j, Wu Q, Gao Z-h, Zhou X. Review on residual stresses in metal additive manufacturing: formation mechanisms, parameter dependencies, prediction and control approaches. *Journal of Materials Research and Technology*. 2022.
6. Edwards P, Ramulu M. Fatigue performance evaluation of selective laser melted Ti–6Al–4V. *Materials Science and Engineering: A*. 2014; 598: 327-37.
7. Fatemi A, Molaei R, Simsiriwong J, et al. Fatigue behaviour of additive manufactured materials: An overview of some recent experimental studies on Ti ‐ 6Al ‐ 4V considering various processing and loading direction effects. *Fatigue & Fracture of Engineering Materials & Structures*. 2019; 42: 991-1009.
8. Xiao Z, Chen C, Zhu H, et al. Study of residual stress in selective laser melting of Ti6Al4V. *Materials & Design*. 2020; 193: 108846.
9. Song X, Feih S, Zhai W, et al. Advances in additive manufacturing process simulation: Residual stresses and distortion predictions in complex metallic components. *Materials & Design*. 2020; 193: 108779.
10. Simson T, Emmel A, Dwars A, Böhm J. Residual stress measurements on AISI 316L samples manufactured by selective laser melting. *Additive Manufacturing*. 2017; 17: 183-9.
11. Phan TQ, Strantza M, Hill MR, et al. Elastic Residual Strain and Stress Measurements and Corresponding Part Deflections of 3D Additive Manufacturing Builds of IN625 AM-Bench Artifacts Using Neutron Diffraction, Synchrotron X-Ray Diffraction, and Contour Method. *Integrating Materials and Manufacturing Innovation*. 2019; 8: 318-34.
12. Barros R, Silva FJ, Gouveia RM, et al. Laser powder bed fusion of Inconel 718: Residual stress analysis before and after heat treatment. *Metals*. 2019; 9: 1290.
13. Teixeira Ó, Silva FJ, Atzeni E. Residual stresses and heat treatments of Inconel 718 parts manufactured via metal laser beam powder bed fusion: an overview. *The International Journal of Advanced Manufacturing Technology*. 2021; 113: 3139-62.
14. Mishurova T, Cabeza S, Thiede T, et al. The Influence of the Support Structure on Residual Stress and Distortion in SLM Inconel 718 Parts. *Metallurgical and Materials Transactions A*. 2018; 49: 3038-46.
15. Ali H, Ma L, Ghadbeigi H, Mumtaz K. In-situ residual stress reduction, martensitic decomposition and mechanical properties enhancement through high temperature powder bed pre-heating of Selective Laser Melted Ti6Al4V. *Materials Science and Engineering: A*. 2017; 695: 211-20.
16. Narvan M, Ghasemi A, Fereiduni E, Kendrish S, Elbestawi M. Part deflection and residual stresses in laser powder bed fusion of H13 tool steel. *Materials & Design*. 2021; 204: 109659.
17. Chiumenti M, Neiva E, Salsi E, et al. Numerical modelling and experimental validation in Selective Laser Melting. *Additive Manufacturing*. 2017; 18: 171-85.
18. Hussein A, Hao L, Yan C, Everson R. Finite element simulation of the temperature and stress fields in single layers built without-support in selective laser melting. *Materials & Design (1980-2015)*. 2013; 52: 638-47.
19. Hodge N, Ferencz R, Solberg J. Implementation of a thermomechanical model in diablo for the simulation of selective laser melting. Lawrence Livermore National Laboratory, Livermore, CA (United States), 2013.
20. Yang X, Barrett RA, Tong M, Harrison NM, Leen SB. Towards a process-structure model for Ti-6Al-4V during additive manufacturing. *Journal of Manufacturing Processes*. 2021; 61: 428-39.
21. Promoppatum P, Uthaisangsuk V. Part scale estimation of residual stress development in laser

powder bed fusion additive manufacturing of Inconel 718. *Finite Elements in Analysis and Design*. 2021; 189.
22. Bayat M, Klingaa CG, Mohanty S, et al. Part-scale thermo-mechanical modelling of distortions in Laser Powder Bed Fusion – Analysis of the sequential flash heating method with experimental validation. *Additive Manufacturing*. 2020; 36.
23. Williams RJ, Davies CM, Hooper PA. A pragmatic part scale model for residual stress and distortion prediction in powder bed fusion. *Additive Manufacturing*. 2018; 22: 416-25.
24. Rolph III WD, Bathe KJ. An efficient algorithm for analysis of nonlinear heat transfer with phase changes. *International Journal for Numerical Methods in Engineering*. 1982; 18: 119-34.
25. Kim S-H, Kim J-B, Lee W-J. Numerical prediction and neutron diffraction measurement of the residual stresses for a modified 9Cr–1Mo steel weld. *Journal of Materials Processing Technology*. 2009; 209: 3905-13.
26. Karayagiz K, Elwany A, Tapia G, et al. Numerical and experimental analysis of heat distribution in the laser powder bed fusion of Ti-6Al-4V. *IISE Transactions*. 2018; 51: 136-52.
27. Cheng B, Shrestha S, Chou K. Stress and deformation evaluations of scanning strategy effect in selective laser melting. *Additive Manufacturing*. 2016; 12: 240-51.
28. Li Y, Zhou K, Tan P, Tor SB, Chua CK, Leong KF. Modeling temperature and residual stress fields in selective laser melting. *International Journal of Mechanical Sciences*. 2018; 136: 24-35.
29. Dassault Systemes. Abaqus Analysis User's Guide. *Abaqus*. 2018.
30. Zhou J, Barrett RA, Leen SB. Three-dimensional finite element modelling for additive manufacturing of Ti-6Al-4V components: Effect of scanning strategies on temperature history and residual stress. *Journal of Advanced Joining Processes*. 2022; 5: 100106.
31. Zhang W, Tong M, Harrison NM. Scanning strategies effect on temperature, residual stress and deformation by multi-laser beam powder bed fusion manufacturing. *Additive Manufacturing*. 2020; 36.
32. Lindgren L. Computational welding mechanics: Thermomechanical and microstructructural simulations. CRC Press/Woodhead Publishing, Boca Raton, Florida/Cambridge, UK, 2007.
33. Zhang W, Tong M, Harrison NM. Multipart Build Effects on Temperature and Residual Stress by Laser Beam Powder Bed Fusion Additive Manufacturing. *3D Printing and Additive Manufacturing*. 2021.
34. Yang Y, Allen M, London T, Oancea V. Residual Strain Predictions for a Powder Bed Fusion Inconel 625 Single Cantilever Part. *Integrating Materials and Manufacturing Innovation*. 2019; 8: 294-304.
35. Khairallah SA, Anderson AT, Rubenchik A, King WE. Laser powder-bed fusion additive manufacturing: Physics of complex melt flow and formation mechanisms of pores, spatter, and denudation zones. *Acta Materialia*. 2016; 108: 36-45.
36. Nycz A, Lee Y, Noakes M, et al. Effective residual stress prediction validated with neutron diffraction method for metal large-scale additive manufacturing. *Materials & Design*. 2021; 205: 109751.
37. Li C, Liu JF, Fang XY, Guo YB. Efficient predictive model of part distortion and residual stress in selective laser melting. *Additive Manufacturing*. 2017; 17: 157-68.
38. Dassault Systemes. Abaqus Analysis User's Guide. *Abaqus*. 2020.
39. Special Metals. Inconel alloy 625. *Special Metals Corporation*. 2013.
40. Wang P, Zhang B, Tan CC, et al. Microstructural characteristics and mechanical properties of carbon nanotube reinforced Inconel 625 parts fabricated by selective laser melting. *Materials & Design*. 2016; 112: 290-9.
41. Anca A, Fachinotti VD, Escobar‐Palafox G, Cardona A. Computational modelling of shaped metal deposition. *International journal for numerical methods in engineering*. 2011; 85: 84-106.
42. Yang Q, Zhang P, Cheng L, Min Z, Chyu M, To AC. Finite element modeling and validation of thermomechanical behavior of Ti-6Al-4V in directed energy deposition additive manufacturing. *Additive Manufacturing*. 2016; 12: 169-77.
43. National Institute of Standards and Technology (NIST). "2018 AM-Bench Test Descriptions for AMB2018-01". 2018.
44. Ahmad B, van der Veen SO, Fitzpatrick ME, Guo H. Residual stress evaluation in selective-laser-melting additively manufactured titanium (Ti-6Al-4V) and inconel 718 using the contour method

and numerical simulation. *Additive Manufacturing*. 2018; 22: 571-82.
45. Ahn D-G. Directed energy deposition (DED) process: state of the art. *International Journal of Precision Engineering and Manufacturing-Green Technology*. 2021; 8: 703-42.
46. Soundararajan B, Sofia D, Barletta D, Poletto M. Review on modeling techniques for powder bed fusion processes based on physical principles. *Additive Manufacturing*. 2021; 47: 102336.
47. Keller N, Ploshikhin V. New Method for Fast Predictions on Residual Stress and Distortion of AM Parts. *2014 International Solid Freeform Fabrication Symposium*: University of Texas at Austin, 2014.
48. Ganeriwala R, Strantza M, King W, et al. Evaluation of a thermomechanical model for prediction of residual stress during laser powder bed fusion of Ti-6Al-4V. *Additive Manufacturing*. 2019; 27: 489-502.
49. Costa L, Vilar R, Reti T, Deus A. Rapid tooling by laser powder deposition: Process simulation using finite element analysis. *Acta Materialia*. 2005; 53: 3987-99.
50. Huang H, Ma N, Chen J, Feng Z, Murakawa H. Toward large-scale simulation of residual stress and distortion in wire and arc additive manufacturing. *Additive Manufacturing*. 2020; 34: 101248.
51. Papadakis L, Loizou A, Risse J, Bremen S, Schrage J. A computational reduction model for appraising structural effects in selective laser melting manufacturing. *Virtual and Physical Prototyping*. 2014; 9: 17-25.
52. Jimenez X, Dong W, Paul S, Klecka MA, To AC. Residual stress modeling with phase transformation for wire arc additive manufacturing of B91 steel. *Jom*. 2020; 72: 4178-86.
53. Salvati E, Korsunsky A. Micro-scale measurement & FEM modelling of residual stresses in AA6082-T6 Al alloy generated by wire EDM cutting. *Journal of Materials Processing Technology*. 2020; 275: 116373.
54. Mirkoohi E, Tran H-C, Lo Y-L, Chang Y-C, Lin H-Y, Liang SY. Mechanics Modeling of Residual Stress Considering Effect of Preheating in Laser Powder Bed Fusion. *Journal of Manufacturing and Materials Processing*. 2021; 5.
55. Cao J, Gharghouri MA, Nash P. Finite-element analysis and experimental validation of thermal residual stress and distortion in electron beam additive manufactured Ti-6Al-4V build plates. *Journal of Materials Processing Technology*. 2016; 237: 409-19.
56. Lu X, Lin X, Chiumenti M, et al. Residual stress and distortion of rectangular and S-shaped Ti-6Al-4V parts by Directed Energy Deposition: Modelling and experimental calibration. *Additive Manufacturing*. 2019; 26: 166-79.
57. Vrancken B, Buls S, Kruth JP, Humbeeck JV. Preheating of selective laser melted Ti6Al4V: microstructure and mechanical properties. *Proceedings of the 13th World Conference on Titanium*: Wiley Online Library, 2016, p. 1269-77.
58. Wang W, Lin W, Yang R, et al. Mesoscopic evolution of molten pool during selective laser melting of superalloy Inconel 738 at elevating preheating temperature. *Materials & Design*. 2022; 213: 110355.
59. Poulin J-R, Brailovski V, Terriault P. Long fatigue crack propagation behavior of Inconel 625 processed by laser powder bed fusion: Influence of build orientation and post-processing conditions. *International Journal of Fatigue*. 2018; 116: 634-47.
60. Hua Y, Liu Z. Experimental investigation of principal residual stress and fatigue performance for turned nickel-based superalloy Inconel 718. *Materials*. 2018; 11: 879.
61. Yang X, Barrett RA, Harrison NM, Leen SB. A physically-based structure-property model for additively manufactured Ti-6Al-4V. *Materials & Design*. 2021; 205: 109709.
62. Zhang Q, Xie J, Gao Z, London T, Griffiths D, Oancea V. A metallurgical phase transformation framework applied to SLM additive manufacturing processes. *Materials & Design*. 2019; 166: 107618.